Three-Dimensional Computational Modeling of Subject-Specific Cerebrospinal Fluid Flow in the Subarachnoid Space

Sumeet Gupta
Laboratory of Thermodynamics in Emerging Technologies,
Department of Mechanical and Process Engineering,
ETH Zurich,
8092 Zurich, Switzerland

Michaela Soellinger

Peter Boesiger

Institute for Biomedical Engineering,
University of Zurich,
CH-8006 Zurich, Switzerland;
ETH Zurich,
8092 Zurich, Switzerland

Dimos Poulikakos
e-mail: dimos.poulikakos@ethz.ch

Vartan Kurtcuoglu[1]
e-mail: vartan.kurtcuoglu@ethz.ch

Laboratory of Thermodynamics in Emerging Technologies,
Department of Mechanical and Process Engineering,
ETH Zurich,
8092 Zurich, Switzerland

This study aims at investigating three-dimensional subject-specific cerebrospinal fluid (CSF) dynamics in the inferior cranial space, the superior spinal subarachnoid space (SAS), and the fourth cerebral ventricle using a combination of a finite-volume computational fluid dynamics (CFD) approach and magnetic resonance imaging (MRI) experiments. An anatomically accurate 3D model of the entire SAS of a healthy volunteer was reconstructed from high resolution T2 weighted MRI data. Subject-specific pulsatile velocity boundary conditions were imposed at planes in the pontine cistern, cerebellomedullary cistern, and in the spinal subarachnoid space. Velocimetric MRI was used to measure the velocity field at these boundaries. A constant pressure boundary condition was imposed at the interface between the aqueduct of Sylvius and the fourth ventricle. The morphology of the SAS with its complex trabecula structures was taken into account through a novel porous media model with anisotropic permeability. The governing equations were solved using finite-volume CFD. We observed a total pressure variation from −42 Pa to 40 Pa within one cardiac cycle in the investigated domain. Maximum CSF velocities of about 15 cm/s occurred in the inferior section of the aqueduct, 14 cm/s in the left foramen of Luschka, and 9 cm/s in the foramen of Magendie. Flow velocities in the right foramen of Luschka were found to be significantly lower than in the left, indicating three-dimensional brain asymmetries. The flow in the cerebellomedullary cistern was found to be relatively diffusive with a peak Reynolds number (Re)=72, while the flow in the pontine cistern was primarily convective with a peak Re=386. The net volumetric flow rate in the spinal canal was found to be negligible despite CSF oscillation with substantial amplitude with a maximum volumetric flow rate of 109 ml/min. The observed transient flow patterns indicate a compliant behavior of the cranial subarachnoid space. Still, the estimated deformations were small owing to the large parenchymal surface. We have integrated anatomic and velocimetric MRI data with computational fluid dynamics incorporating the porous SAS morphology for the subject-specific reconstruction of cerebrospinal fluid flow in the subarachnoid space. This model can be used as a basis for the development of computational tools, e.g., for the optimization of intrathecal drug delivery and computer-aided evaluation of cerebral pathologies such as syrinx development in syringomelia. [DOI: 10.1115/1.3005171]

Keywords: cerebrospinal fluid, subarachnoid space, porous media, MRI, drug delivery

1 Introduction

The cerebrospinal fluid (CSF) is a colorless fluid that surrounds the brain and spinal cord [1]. It circulates in the ventricles and the subarachnoid space, carrying away potentially harmful metabolites, transporting hormones, and cushioning the brain. CSF is produced mainly by the choroid plexus in the lateral, third, and fourth ventricles. It flows from the lateral ventricles to the third ventricle via the foramina of Monro. From the third ventricle, CSF passes into the fourth ventricle through the aqueduct of Sylvius and flows out of the fourth ventricle through the midline foramen of Magendie and the lateral foramina of Luschka into the subarachnoid space, which comprises a network of interconnected cisterns. Some fluid passes downward into the spinal cavity, but most of the fluid flows upward around the tentorium to be absorbed mainly through the arachnoid granulations into the superior sagittal sinus. Figure 1 illustrates the flow path of CSF within the intracranial cavities.

In addition to the customary associations of CSF flow pathology with diseases such as hydrocephalus, multiple sclerosis, cryptoccocal meningitis, and Alzheimer's disease [2,3], the study of CSF circulation has gained a more recent interest due to its function as a transport medium of the brain [4,5]. For the delivery of therapeutic drugs that cannot cross the blood brain barrier, direct injection into the CSF space can be used as an alternative pathway [6–12]. Other advantages of intrathecal or intracerebroventricular drug injection are reduced dosage compared to systemic injection and enhanced drug half-life due to low chemical binding of CSF with the drug molecules [6]. Morphine injection into the intrathecal cavity is particularly effective, because the drug does not have to circulate systemically to reach the periacqueductal gray

[1]Corresponding author.

Contributed by the Bioengineering Division of ASME for publication in the JOURNAL OF BIOMECHANICAL ENGINEERING. Manuscript received October 23, 2007; final manuscript received August 25, 2008; published online December 10, 2008. Review conducted by Philip V. Bayly.

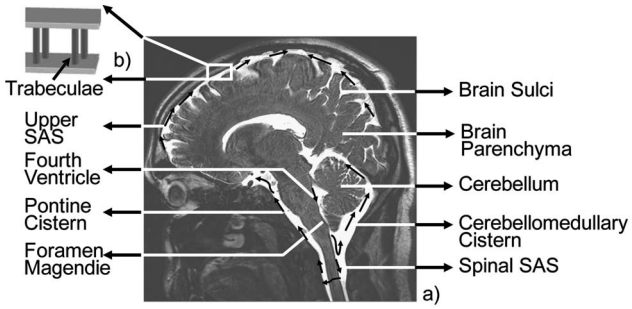

Fig. 1 (*a*) CSF space anatomy (T2 weighted MRI image) and pathways in the intracranial cavities. (*b*) Schematic of trabeculae bridging the SAS between arachnoid and pia layers.

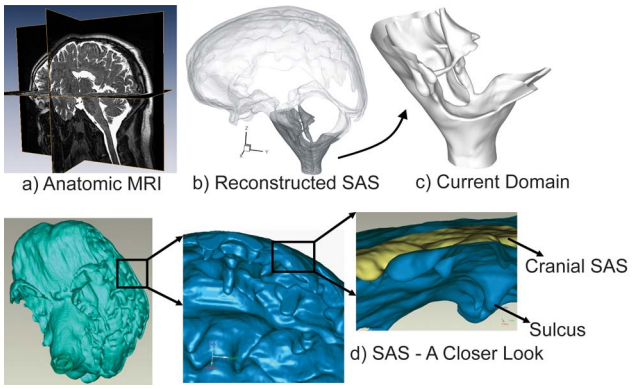

Fig. 2 3D reconstruction of the SAS using anatomic MRI. (*a*) Anatomical MRI slices were segmented to produce (*b*) a 3D model of the SAS. (*c*) The current investigation domain. (*d*) Detailed anatomy of the superior cranial SAS.

(region toward anterior of cerebral acqueduct) and dorsal spine, where μ-opioid receptors are present [7,8]. Together with reduced dosage (reduction of up to 200% as compared to oral or systemic morphine dose), the intrathecal morphine gives enhanced pain control with minimal side effects [9]. There are various other clinically relevant drugs such as 9-nitro-camptothecin (9NC) for the treatment of neoplastic meningitis [10], baclofen for treatment of spasticity of cerebral origin [11], and thyrotropin releasing hormone for the treatment of amytrophic lateral sclerosis [12], where intrathecal drug delivery is warranted and where the knowledge of CSF dynamics may allow efficient drug delivery procedures. There are several other applications, such as shunt treatment of hydrocephalus [13] and pathogenesis of syringomelia [14,15], where comprehensive knowledge of CSF pathways, pressure, and the associated dynamics is required for improved diagnosis and treatment. With the steady improvement of medical imaging techniques such as magnetic resonance imaging (MRI), it has become possible to capture CSF flow rates and velocities at specific locations. However, the noninvasive measurement of intracranial pressure (ICP) remains an unresolved issue.

A variety of lumped parameter and electric resistance models are available in literature [16–18] that calculate CSF dynamics based on flow parameters estimated using zero-dimensional approximation of the system. While these models are suitable for a general understanding of CSF flow within the cranium, their value for clinical applications is limited. A handful of computational fluid dynamics (CFD) models that provide subject-specific quantitative description of CSF flow have been published [19–25]. However, most of these models investigate CSF dynamics only in the ventricular space. Despite its irrefutable significance, there has been almost no effort to extend these models to the surrounding subarachnoid space (SAS). The principal reason for this is the complexity of the SAS, both in terms of anatomy and the flow field, as well as the lack of sufficient information from clinical flow measurements. Jacobson et al. [26] were the first to estimate CSF flow resistance in the SAS based on a computational model. However, their investigation was based on an idealized and extensively simplified representation of the SAS. Loth et al. [27] provided a detailed description of fluidic characteristics based on their anatomically accurate model of the spinal subarachnoid space. Stockman [28] performed lattice Boltzmann simulations to describe oscillatory flow in the spinal SAS and also estimated the effect of trabecula network bridging this space. However, the investigations of Loth et al. [27] and Stockman [28] were limited to the spinal CSF space. To the best of our knowledge, the only work that deals with CSF flow in the cranial subarachnoid space and the fourth ventricle using the fluid mechanics principles is the work by Zhu et al. [29] and Linninger et al. [30,31]. Their analysis predicts pulsatile CSF dynamics in the normal and hydrocephalic brain. However, their work do not take into account the three dimensional CSF dynamics and is restricted to two dimensional flow field analysis computed over the midsaggital plane.

The presence of a complex weblike trabecula network in the SAS complicates the investigation of the flow field [32]. Figure 1(*b*) shows the schematic of trabecula structure bridging the SAS between arachnoid and pia layers. These trabeculae may exhibit a considerable variability in terms of number and structure, depending on their location in the SAS. The mechanical role of the trabeculae is twofold: they help reduce CSF pressure on the brain parenchyma by providing resistance to CSF flow, and they damp brain acceleration, preventing the brain from hitting the rigid skull. Jacobson et al. [26] modeled bulk CSF flow, treating the SAS as a porous medium with uniform properties. While the porosity of the SAS is estimated to be around 0.99 [33], there are no published values on its permeability. In the calculations of Jacobson et al. [26], a range of permeability values varying from 8×10^{-3} m^2 to 8×10^{-10} m^2 was chosen to determine the pressure loss in SAS due to the presence of trabeculae. Since the trabecula structures extend longitudinally from the arachnoid to the pia layer (see Fig. 1(*b*)), the permeability along the longitudinal axis of the trabeculae may differ significantly compared to the permeability in the transverse direction. In the work at hand, we present an anisotropic porous media model for the SAS that takes into account directional variations of SAS permeability.

We have taken into account the accurate three-dimensional anatomy of the SAS based on MRI data. We have investigated the CSF flow in the inferior cranial and superior spinal SAS keeping in mind its clinical relevance exemplified by intrathecal drug delivery [6–12], and diagnosis of syrinxes in syringomelia [14,15] and chiari malformation [34] due to the elongation of cerebellar tonsils into the SAS. We have performed the investigation using computational fluid dynamics with pulsatile subject-specific BCs derived from velocimetric MRI. The anisotropic porous media model, the anatomically accurate SAS description, and three-dimensional transient simulations based on MRI boundary conditions are novel. To the best of our knowledge, the work at hand is the first published effort to investigate subject-specific CSF dynamics in the three-dimensional subarachnoid space.

2 Method

2.1 Acquisition of Subarachnoid Space Anatomy. The three-dimensional anatomy of the SAS was reconstructed from a total of 230 T2 weighted MRI images by manual image segmentation (Fig. 2). The images covering the entire brain were acquired in sagittal direction on a 3T MRI scanner (Achieva, Philips Medical Systems, Best, The Netherlands). The in plane resolution was 0.45×0.45 mm^2 and the slice spacing was 0.6 mm. For readout, a high resolution 3D turbo spin-echo sequence with an echo time (TE)=150 ms, repetition time (TR)=2000 ms, and a flip angle of 90 deg was used. The scan was performed on a 25 years old

healthy male volunteer. The T2 weighted scans ensure a good contrast between brain tissue and the CSF space, the latter appearing as a white region in the scans (Fig. 2(*a*)).

The segmentation was carried out manually on each MR slice in coronal, sagittal, and transverse directions using AMIRA 3.1.1 (Mercury Computer Systems/TGS, San Diego, CA). A polygonal surface model of the three-dimensional SAS was then reconstructed based on the segmented images (Fig. 2(*b*)), capturing the intricate details of the brain surface. This is necessary, as the presence of brain sulci (Fig. 2(*d*)) will significantly affect the CSF flow behavior in the cranial subarachnoid space. The treated cerebral structures, namely, cerebrum, cerebellum, fourth ventricle, spinal cord, and the subarachnoid space, were segmented separately and subsequently registered in order to enhance the accuracy of the reconstruction process. Smoothing was performed on each MRI slice using a modified Gaussian filter with a filter mask of 5×5 pixels. In order to eliminate segmentation artifacts, the segmented model was smoothed once more in 3D and fitted with nonuniform rational Bézier spline (NURBS) surfaces. NURBS inherently assume double derivative continuity on the model surface, thus providing an excellent basis for CFD grid generation. The file size was reduced tenfold with the NURBS representation. This was essential in order to make the geometry tractable for further investigation. With a mean value of 0.01 mm, the deviation of the NURBS representation from the anatomic segmentation was well within acceptable limits.

2.2 MRI Acquisition of CSF Flow. The boundary conditions for the CFD simulations were obtained using velocity-encoded MRI. Through plane velocities were measured at three transverse planes in the subarachnoid space: at the foramen magnum in the spinal canal, in the pontine cistern, and in the cerebellomedullary cistern (Fig. 3). Phase contrast velocity imaging combined with an ECG triggered T1-weighted transient field echo (TFE) read-out scheme was applied. In plane scan resolution was 0.46×0.46 mm^2; slice thickness was 6 mm for the spinal canal and 5 mm for the pontine and the cerebellomedullary cisterns. For measurements in cerebellomedullary cistern, the phase encoding velocity was set to 2 cm/s, 4 cm/s for pontine cistern, and 7 cm/s for the spinal canal. Voxels of interest were manually extracted on the magnitude images, where CSF is displayed as white and brain tissue as gray. Before further postprocessing, phase unwrapping was performed in the pontine cistern and the signals originating from blood vessels within the cavity were extracted by hard threshholding on the phase images.

The measured profiles were filtered using a median filter [35] with a filter mask of 5×5 pixels. The filtered profiles were subsequently smoothed using cubic spline interpolation on a uniform mesh created in MATLAB 7.1 (The Mathworks, Inc., Natick, MA). The interpolation from the uniform mesh onto the computational mesh for the subsequent CFD simulations was performed using the E02DCF and E02DEF libraries of the NAG Toolbox for MATLAB (Numerical Algorithms Group Ltd., Oxford, UK). Figure 3 shows the interpolated profiles at all treated boundaries.

2.3 Computational Model. The CSF motion in the SAS can be described by a system of partial differential equations that conserve mass and momentum. Under normal physiological conditions, the CSF behaves as an incompressible Newtonian fluid with density and viscosity same as that of water at 37°C [24]. The governing equations for mass and momentum conservation can then be, respectively, written as follows.

In continuity equation,

$$\rho(\nabla\cdot\boldsymbol{u})=\dot{S}_m \tag{1}$$

In momentum (Navier–Stokes) equations,

$$\rho\left(\frac{\partial\boldsymbol{u}}{\partial t}+\boldsymbol{u}\cdot\nabla\boldsymbol{u}\right)=-\nabla p+\mu\nabla^2\boldsymbol{u}+\boldsymbol{S}_P \tag{2}$$

where $\boldsymbol{u}$ is the velocity vector, p is the fluid pressure, ρ is the CSF density, μ is the CSF viscosity, $\dot{S}_m$ is the rate of CSF generation per unit volume in the fourth ventricle (Eq. (7)), and $\boldsymbol{S}_P$ is the pressure gradient due to trabecular morphology of the SAS (Eq. (3)). The contributions of the third and lateral ventricle choroid plexus to CSF production are taken into account through boundary conditions as specified in Sec. 2.4. In order to incorporate the effect of trabeculae on the flow field, the entire domain—with exception of the fourth ventricle and the foramen of Luschka—was modeled as a Brinkman porous medium [36]. The pressure drop caused by the porous medium, known as Darcy's drag, was modeled by the addition of a resistive momentum source term $\boldsymbol{S}_P$ to the Navier–Stokes equations. $\boldsymbol{S}_P$ was formulated using Darcy's law that relates the flow velocity linearly to the pressure gradient within the porous domain,

$$S_{P,i}=\left(-\sum_{j=1}^{3}D_{ij}\mu u_j\right),\quad \boldsymbol{S}_P=\begin{Bmatrix}S_{P,1}\\S_{P,2}\\S_{P,3}\end{Bmatrix} \tag{3}$$

where $S_{P,i}$ is the source term for the ith (x, y, or z) momentum equation and D_{ij} is a second order flow resistance tensor, as defined in Eq. (6) in Sec. 2.3.1. D_{ij} represents the resistance to CSF flow due to the presence of trabeculae and is mathematically equal to the inverse of the permeability tensor k_{ij} (see Sec. 2.3.1). Equations (2) and (3) can be combined to yield the Navier–Stokes/Brinkman equations:

$$\rho\left(\frac{\partial\boldsymbol{u}}{\partial t}+\boldsymbol{u}\cdot\nabla\boldsymbol{u}\right)=-\nabla p+\mu\nabla^2\boldsymbol{u}-c\left(\sum_{j=1}^{3}D_{ij}\mu u_j\right) \tag{4}$$

where

$$c=\begin{cases}0 & \text{fourth ven tricle foramen of Luschka}\\ 1 & \text{subarachnoid space}\end{cases}$$

2.3.1 Estimation of SAS Permeability. For the estimation of SAS permeability tensor k_{ij}, the porous subarachnoid space was assumed to feature an idealized morphology, as shown in Fig. 4(*a*). The upper wall in Fig. 4(*a*) represents the arachnoid layer and the lower wall represents the pia layer. The trabeculae were assumed to be straight cylindrical pillars extending normally to the arachnoid layer. This simplified trabecular representation for the SAS can be compared to a bed with unidirectional fibers, for which the closed form solutions for permeability in arbitrary direction can be derived using the approach of Westhuizen and Du Plessis [37]. This methodology is founded on the phase average form of the Navier–Stokes equation over a representative unit cell (RUC). The RUC is defined as the smallest volume containing a single pore that still captures the details of the fibrous structure. The underlying principle here is similar to the periodic unit cell approach of Boomsma et al. [38], where the authors modeled flow through open cell metal foams. This approach allows permeability in the RUC to be analytically determined using simple fluid dynamic principles and to be applied to the entire domain comprising of numerous cells of identical morphology. A schematic RUC for the present SAS model is shown in Fig. 4(*b*). The permeability derivation for unidirectional fiber arrangement inherently assumes isotropy in the transverse plane, i.e., $k_{22}=k_{33}$, where 2 and 3 refer to the transverse axes of the trabeculae (Fig. 4(*b*)). For laminar or creep flow through cylindrical fiber structures with fiber radius r and porosity ε, Westhuizen and Du Plessis derived the analytical relations for the longitudinal permeability k_{11} and the transverse permeabilities $k_{22}=k_{33}$ as

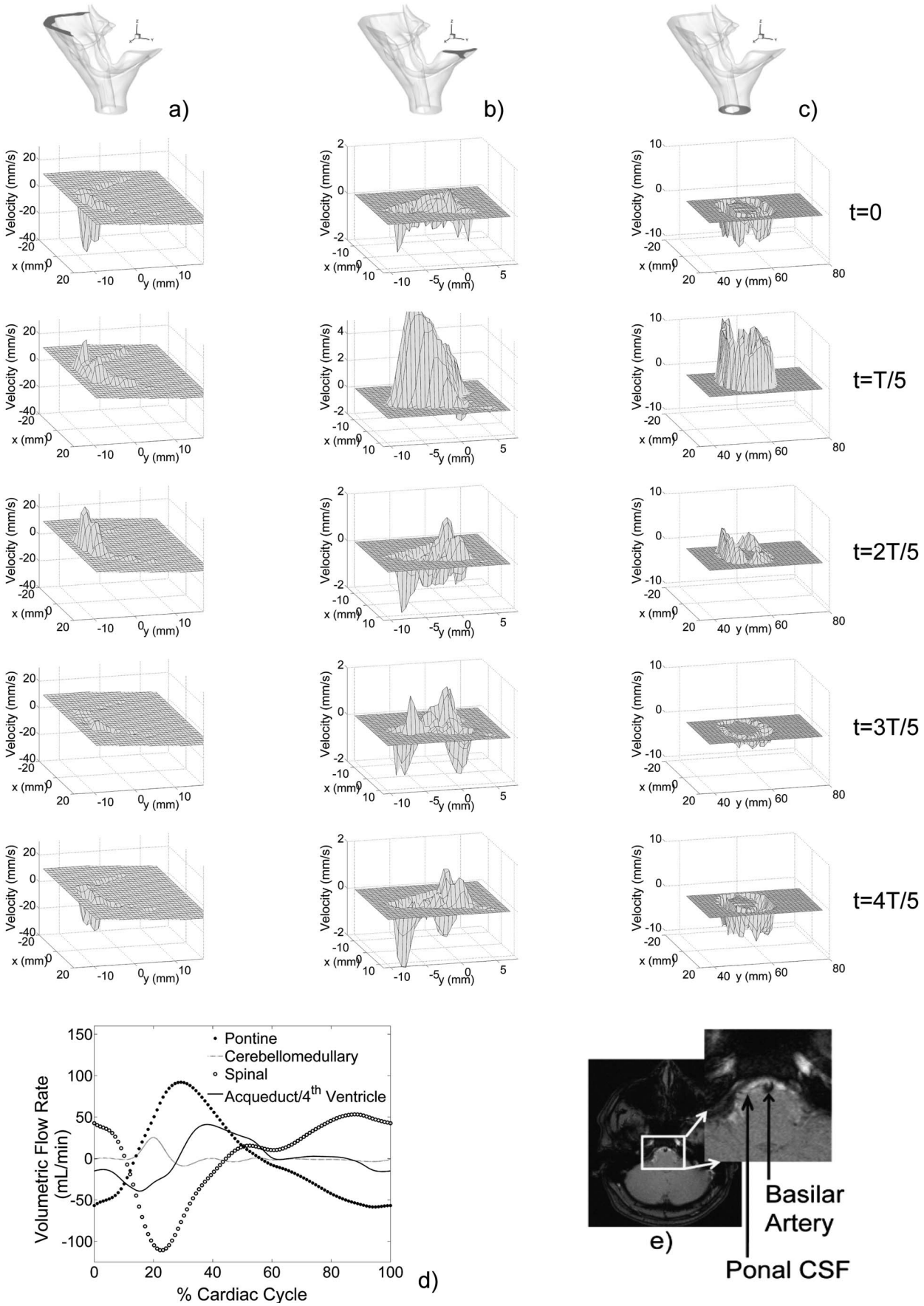

Fig. 3 Velocity profiles at the boundaries as obtained using velocimetric MRI at (*a*) the pontine cistern, (*b*) the cerebellomedullary cistern, and (*c*) the spinal SAS. (*d*) Measured volumetric flow rates at each boundary. (*e*) Magnitude image at pontine cistern with segmented basilar artery.

$$\frac{k_{11}}{r^2} = \frac{\varepsilon^2 \cdot (\pi + 2.157 \cdot (1-\varepsilon))}{48 \cdot (1-\varepsilon)^2}, \quad \frac{k_{22}}{r^2} = \frac{k_{33}}{r^2} = \frac{\pi \cdot \varepsilon \cdot (1-\sqrt{1-\varepsilon})^2}{24 \cdot (1-\varepsilon)^{3/2}} \tag{5}$$

These relations hold true for randomly positioned trabeculae, as in the case of SAS, and are only a function of SAS porosity and the fiber structure (fiber shape and radius). Furthermore, these relations can be easily extended to other physical geometries such as elliptical trabeculae or trabeculae of irregular shapes [39]. Figure 4(*c*) shows the longitudinal and transverse permeabilities as a function of SAS porosity. For the SAS porosity value of $\varepsilon = 0.99$ [33] and trabeculae radius $r = 15$ μm [28], the longitudinal permeability calculated with Eq. (5) is almost six times the transverse permeability, indicating a strong anisotropic nature of the system. The flow resistance tensor D_{ij} can then be defined as

$$D_{ij} \cdot r^2 = \begin{vmatrix} \frac{48 \cdot (1-\varepsilon)^2}{\varepsilon^2 \cdot (\pi + 2.157 \cdot (1-\varepsilon))} & 0 & 0 \\ 0 & \frac{24 \cdot (1-\varepsilon)^{3/2}}{\pi \cdot \varepsilon \cdot (1-\sqrt{1-\varepsilon})^2} & 0 \\ 0 & 0 & \frac{24 \cdot (1-\varepsilon)^{3/2}}{\pi \cdot \varepsilon \cdot (1-\sqrt{1-\varepsilon})^2} \end{vmatrix} \tag{6}$$

For the CFD simulations, D_{ij} was calculated at each location within the SAS. D_{11} represents the resistance to CSF flow normal to the arachnoid layer and $D_{22} = D_{33}$ are the transverse resistances.

2.4 Implementation. The range of length scales in the SAS spans three orders of magnitude, which, together with the pulsatile nature of the CSF flow, necessitate a fine spatial discretization and local control over the computational cell size for the CFD calculations. It must be noted, however, that the increase in number of grid cells exponentially imposes a limit to the computational cost and time. A significant amount of effort was thus spent to create an efficient computational grid that not only accurately resolves the flow field but at the same time keeps calculation cost and times at bay. This multiblock structured hexahedral grid with approximately 4.7×10^6 cells was constructed using ANSYS ICEM CFD (Ansys Inc., Canonsburg, PA). The treated domain was divided up in different regions based on characteristic sizes of geometric features. Grid generation was performed on each region separately, and nonconformal interfaces were used to connect them. For laminar flow such as that of CSF in the SAS, the maximum velocity gradients occur in the boundary layers. It is distinctly necessary to capture these gradients in order to predict accurate flow patterns. Our mesh uses an O-grid inflation layer from all walls so that the mesh is nearly orthogonal and allows for excellent control over near-wall spacing in order to accurately capture velocity gradients in the boundary layers. The height of the inflation layer was approximately determined using the laminar scaling law, $\delta = L \cdot \mathrm{Re}_L^{-1/2}$, where δ is the boundary layer thickness, L is the region-dependent characteristic length, and Re_L is the Reynolds number.

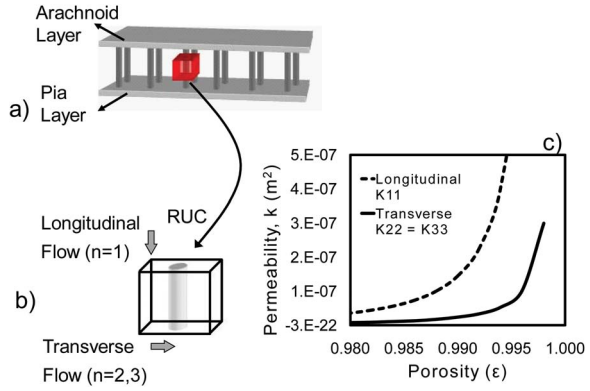

Fig. 4 Porous media representation of the SAS, (*a*) Representative porous model for CFD, (*b*) Representative unit cell and permeability directions, (*c*) permeability variation with porosity (The number of "RUCs" across a channel can be more than one)

The commercial finite volume solver FLUENT 6.3 (Fluent Inc., Lebanon, NH) was used to carry out the computations. The porous media model of the SAS and the transient velocity boundary conditions were implemented in FLUENT by means of user-defined functions. The longitudinal and transverse permeabilities were specified locally with respect to the local coordinate axes rather than relative to the fixed geometric axes of the model. The fluid equations were discretized using a second order upwind scheme [40] in space and second order implicit scheme in time. The second order discretizations were used to enhance the accuracy and robustness of the CFD simulations. The advantage of fully implicit time discretization is that it is unconditionally stable with respect to the time step size. Pressure-velocity coupling was achieved with the SIMPLEC algorithm [41]. The gradients of velocity and pressure were calculated using the Green–Gauss node based gradient evaluation scheme [42]. This scheme reconstructs exact values of a linear function at a node from surrounding cell-centered values on meshes by solving a constrained minimization problem, preserving a second order spatial accuracy.

Subject-specific pulsatile and spatially varying velocity profiles were imposed at the outlet boundaries (namely, pontine cistern, cerebellomedullary cistern, and spinal SAS). These profiles were obtained using velocimetric MRI technique as described in Sec. 2.2. A zero total pressure boundary condition was imposed at the superior entrance of the fourth ventricle. To account for the production of CSF in the fourth ventricle, a mass source $\dot{S}_m$ with zero initial momentum was introduced in the fluid flow equations. $\dot{S}_m$ corresponds to the amount of CSF generated per unit time and per unit volume in the fourth ventricle. The mass source was only added in the inferior part of the fourth ventricle with volume V_{FV}, where choroid plexus is assumed to be present [43]. While there is no common consensus in the community on the amount of CSF being produced in the fourth ventricle, for the present investigation, this value was assumed to be 5% of the overall CSF production $\dot{V}_{\mathrm{CSF,net}}$ [44]. The overall CSF production was calculated by superimposing volumetric flow rates at the outlet boundaries and calculating net flow rate over a cardiac cycle. Here it was assumed that there is no seepage of CSF through the ventricular or sub-

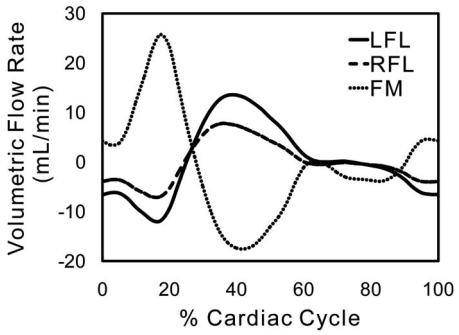

Fig. 5 CSF volumetric flow rates from CFD simulations at LFL, RFL, and FM

arachnoid walls and that 95% of CSF is produced in the lateral and the third ventricles. The mass source $\dot{S}_m$ representing CSF production in fourth ventricle can then be written as

$$\dot{S}_m = 0.05 \cdot \frac{\rho \dot{V}_{\mathrm{CSF,net}}}{V_{\mathrm{FV}}} \tag{7}$$

Independence studies were carried out to ensure that the CFD solution is independent of the spatial grid size and the temporal discretization. Details are given in Appendix A.

3 Results

While the CSF flow in the SAS domain was laminar throughout, a wide variety of interesting flow patterns were observed. The flow field in the left foramen of Luschka (LFL) was found to be considerably different from that in the right foramen of Luschka (RFL), indicating asymmetry in the global CSF flow. This can be explained by the presence of macroscopic and microscopic structural asymmetries in the brain [45]. The anisotropic mechanical properties of brain tissue [41] are likely to amplify the effect of these structural asymmetries on CSF flow by causing a nonuniform deformation of the cerebrospinal fluid space. In the present work, we have taken into account such inhomogeneities through asymmetric velocity boundary conditions. Figure 5 shows the transient volumetric flow rate variation during one cardiac cycle at the midline and lateral recesses of the fourth ventricle. The maximum volumetric flow rate through LFL was 13.1 ml/min, while the maximum flow rate through the RFL was 7.4 ml/min. Figure 6 shows the normal velocity contours at LFL during the entire cardiac cycle (with time period T). High velocities were observed at the foramen of Magendie (FM), peaking at 9.5 cm/s during the first quarter of the cardiac cycle. Table 1 lists the maximum volumetric flow rates, stroke volume, peak velocities, and Reynolds numbers at various channels within the SAS. Stroke volume was calculated by integrating the area under the transient volumetric flow rate curve at the respective channel. The integration was performed separately for systolic and diastolic phases. The mean of the absolute value of these two measurements is the stroke volume. The net CSF production rate, including the production in the fourth ventricle, was 0.47 ml/min or 679 ml/day. This is well within the range of published values [46,47].

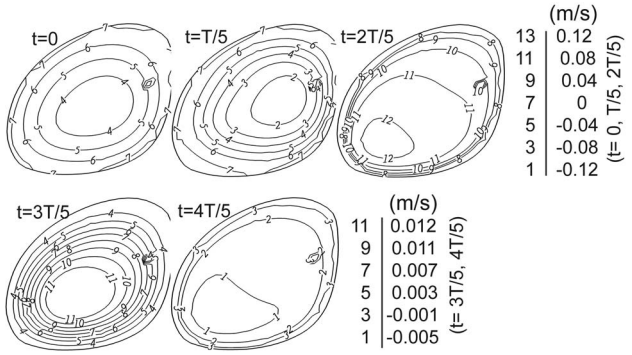

Fig. 6 Normal velocity (m/s) contours at LFL

Table 1 Volumetric flow rates, stroke volume, peak velocities, and Reynolds number at key cross sections within the SAS

	$V_{1,\max}$	$V_{2,\max}$	SV	$\vartheta_{\mathrm{peak}}$	D_H	$\mathrm{Re}_{\mathrm{peak}}$
Aqueduct/fourth ventricle	38.2	44.5	117.20	14.6	1.86	393
Left foramen of Luschka	13.5	11.8	41.05	14.39	1.37	286
Right foramen of Luschka	7.1	7.7	23.99	6.76	1.52	149
Foramen of Magendie	17.5	25.7	57.78	9.49	1.60	220
Spinal subarachnoid	52.8	108.9	271.55	1.40	6.62	134
Cisternal boundary	17.9	6.44	38.64	0.83	6.00	72
Ponal Boundary (Forebrain)	94.7	57.7	289.30	4.28	6.23	386

$V_{1,\max}$=maximum volumetric flow rate in net CSF flow direction (ml/min)
$V_{2,\max}$=maximum volumetric flow rate opposite to the net CSF flow direction (ml/min)
SV=stroke volume (μl)
$\vartheta_{\mathrm{peak}}$=peak flow velocity (cm/s)
D_H=hydrulic diameter of the boundary (mm)
$\mathrm{Re}_{\mathrm{peak}}$=peak Reynolds number based on hydraulic diameter of the boundary

Being a large dilation in the SAS, the basal cerebellomedullary cistern acts as the single most important distribution zone for the CSF communicating between ventricles and the subarachnoid space. Figure 7 shows the stream traces of massless virtual particles injected at Plane A at different cardiac phases. Figure 8 shows the corresponding velocity profiles at different cross sections within the domain. The flow dynamics during one cardiac cycle can be described as follows.

(a) At $t=0$, CSF flows in the cranial direction in the fourth ventricle and in the caudal direction in the SAS. This is caused, presumably, by the expansion of the lateral and third ventricles and the expansion of blood vessels in the SAS and beneath the pia matter or by the compression of the SAS. The latter would indicate that either the trabeculae are compliant or that the compression only occurs locally in areas without the presence of these pillarlike structures.

(b) At $t=\mathrm{T}/5$, CSF continues to flow in cranial direction in the ventricular space, indicating the further expansion of the ventricles. However, the flow in the SAS is no longer in caudal direction but toward the cranial space. This is likely to be caused by the compression of blood vessels in or beneath the SAS or by the expansion of the SAS itself. For overall mass conservation, the flow in the spinal SAS reverses. A jet from the anterior spinal canal enters the narrow ponal region and does not have any bulk space to redistribute. A jet from the posterior spinal canal enters the basal cerebellomedullary cistern and splits into three streams: one entering the foramen of Magendie with a channel-like flow, one rotating around the medulla oblongata and mixing with the jet from the anterior spinal canal, and the third entering the narrow region at the back of the cerebellum (superior cerebellomedullary cistern) and exhibiting very low velocities.

(c) At $t=2\mathrm{T}/5$, the flow in the ventricles is in the caudal

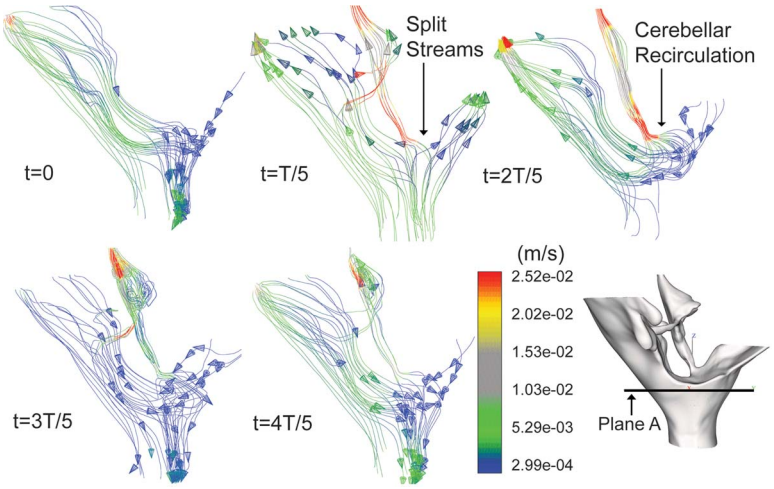

Fig. 7 Stream traces colored by velocity magnitude (m/s). Particles are injected at Plane A intersecting the basal pontine and cerebellomedullary cisterns.

direction, indicating contraction of the ventricular walls. A jet emerging from the aqueduct splits into three streams flowing into each of the lateral and midline recesses of the fourth ventricle. The flow entering the basal cerebellomedullary cistern from the foramen of Magendie and the spinal canal circulates around the medulla to enter the ponal region. At the same time, jets from LFL and RFL also enter the pontine cistern, flow toward the center of the cistern, and are carried upward toward the cranium with the inertia of the flow arriving from the spinal cavity. This behavior of the flow ensures that the CSF arriving from the fourth ventricle and inferior SAS has enough inertia to traverse the entire cranial space and eventually exit through the arachnoid granulations.

(d) At $t=3T/5$, the CSF is virtually dormant in terms of fluid dynamics. The flow velocities in the entire domain are below 5 mm/s, except for a jet appearing in the fourth ventricle. This is likely to be the condition of relaxation of the contracted ventricular walls.

(e) At $t=4T/5$, the expansion of the blood vessels in or beneath the SAS or compression of the SAS begins again, forcing the flow in caudal direction in the SAS and conserving the periodicity of the cycle.

The net and maximum volumetric flow rates observed in the superior cerebellomedullary cistern are 0.13 ml/min and 6.4 ml/min, respectively. The flow in the superior cerebellomedullary cistern resembles a creep flow with a maximum absolute velocity of 0.83 cm/s and a peak Reynolds number of 72 based on the hydraulic diameter of the boundary. At such low Reynolds numbers, the flow can theoretically be represented by only diffusive and Darcy terms in the Navier–Stokes/Brinkman equations (Eq. (4)). As opposed to the flow in the cerebellomedullary cistern, the flow in the fourth ventricle is mostly convective with peak Reynolds number of 393 and a peak velocity of approximately 15 cm/s at the superior end of the fourth ventricle, i.e., in the aqueductal region. Figure 9 shows the velocity magnitude contours in the entire domain within one cardiac cycle. The hornlike protrusions at the posterior section of the fourth ventricle experience only secondary flow outside the influence region of the jet arriving from the aqueduct. The flow velocity remains below 1 cm/s in the horns, while it reaches the order of 10 cm/s toward the anterior wall of the ventricle.

Figure 10 shows the pressure variations within one cardiac cycle. The pressure at any point within the domain is measured as a relative static pressure with respect to the zero total pressure at

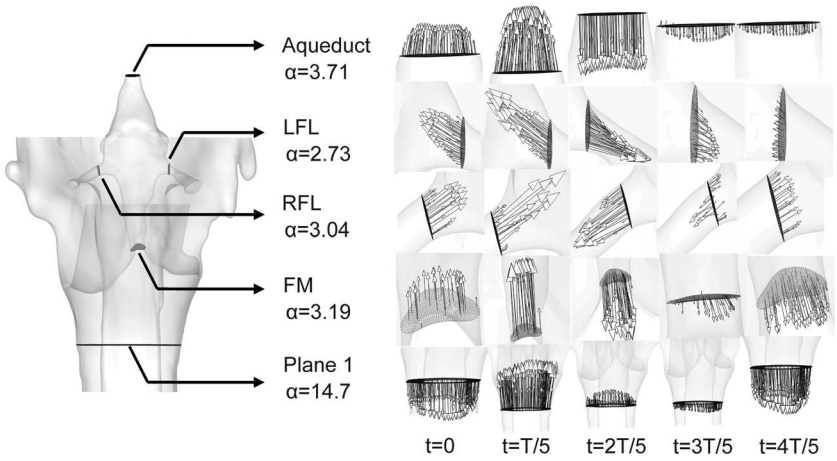

Fig. 8 Velocity profiles at different cross sections within the domain. α is the Womersley number. (Cross sections are scaled differently at different time steps for better representation of the vectors.)

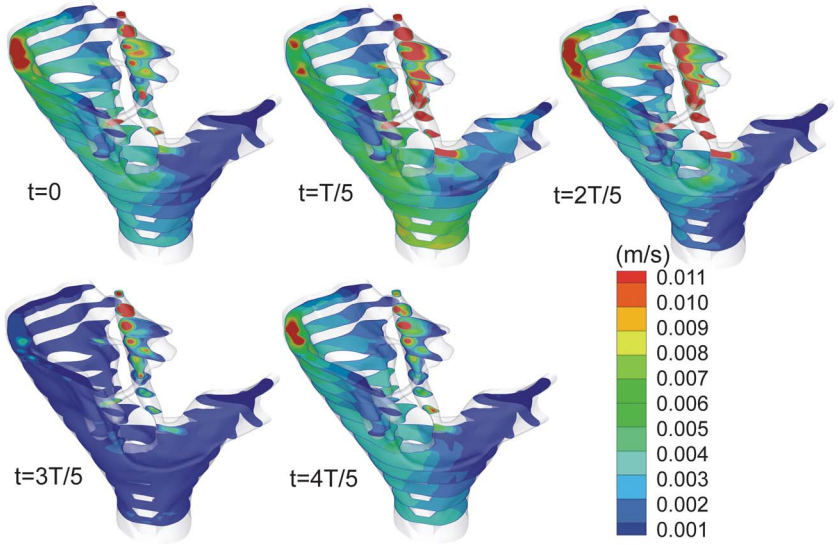

Fig. 9 Velocity magnitude (m/s) contours in the SAS during one complete cardiac cycle (The velocity range in this figure has been chosen in order to best visualize the flow field.)

the superior end of the fourth ventricle. The observed pressure range within one cardiac cycle is from −42 Pa to 40 Pa. Toward the beginning of the cardiac cycle, the pressure throughout the domain is positive with a maximum pressure of less than 35 Pa in the pontine cistern, 39 Pa in the cerebellomedullary cistern, and 15 Pa in the fourth ventricle. The flow reverses direction in the second quarter of the cycle and a complete pressure reversal occurs with lowest the pressure of −42 Pa in the pontine cistern, −23 Pa in the cerebellomedullary cistern, and −12 Pa in the fourth ventricle. During the third quarter, the pressure throughout the domain remains relatively low and uniform indicating relaxation of the ventricular and SAS walls. The second flow reversal occurs toward the latter half of the fourth quarter of the cycle. The total pressure range in the fourth ventricle is from −15 Pa to 15 Pa throughout the cardiac cycle.

4 Discussion

The net volumetric flow rate at the spinal boundary was approximately zero, which corresponds well with the results of Loth et al. [27]. This implies that the spinal cavity principally acts as a conduit for oscillatory CSF flow, cushioning the spinal cord, with none or very little fluid being absorbed within the spinal SAS. The cross-sectional flow profiles in most of the SAS domain were relatively flat in the middle and steeper toward the wall, rather than being parabolic (Fig. 8). Such a flow behavior can be attributed to the effect of transient inertial forces within the CSF system. This can be explained by considering the Womersley parameter α, which is defined as

$$\alpha^2 = \frac{\text{transient inertial force}}{\text{viscous force}} = \frac{\rho \omega r_h^2}{\mu} \tag{8}$$

where $\omega = 2\pi/T$ is the oscillatory flow frequency, T is the time period of the cardiac cycle, ρ and μ are CSF density and viscosity, respectively, and $r_h = 2 \cdot \text{area} \cdot (\text{perimeter})^{-1}$ is the hydraulic radius. For small Womersley numbers ($\alpha < 1$), the transient inertial forces are low and the parabolic velocity profile has sufficient time to develop during each cycle. Hence, the flow remains in phase with the pressure gradient and the parabolic nature of the profiles is preserved. For larger Womersley numbers ($\alpha > 1$), the transient inertial forces are high enough that velocity profiles have little time to respond to the pressure gradient and hence the profiles are relatively flat toward the center. The Womersley number for the flow in Plane 1 (Fig. 8) is rather high, i.e., $\alpha \approx 15$, leading to a velocity profile with a flat center resembling that of plug flow.

CSF pulsation is primarily driven by the motion of ventricular walls, the expansion and contraction of the choroid plexus [48], and the blood vessel motion in the SAS [49], which result from the in- and outflow of blood into the cranial space that has, in adults, a time independent volume. The subarachnoid space is capable of volume change through the deformation of blood vessels located within it. This can be seen clearly when the volumetric flow rate at the spinal cord and the foramina of Luschka and Magendie are considered at $t = 2T/5$ (Fig. 8): CSF enters the cranial subarachnoid space from both the fourth ventricle and the spinal SAS at this point in time, necessitating a compliant cranial SAS. The presence of trabeculae in the subarachnoid space is likely to inhibit global deformation of the pia and arachnoid layers in contrast to the deformation of the ventricle walls. This is, within current technical limitations, confirmed by MRI [50,51]. To place the amplitude of such a potential but unlikely global deformation into perspective, we have calculated the uniform distension of the cranial SAS that would be required to accommodate the influx of CSF into the cranial SAS as a function of time, as

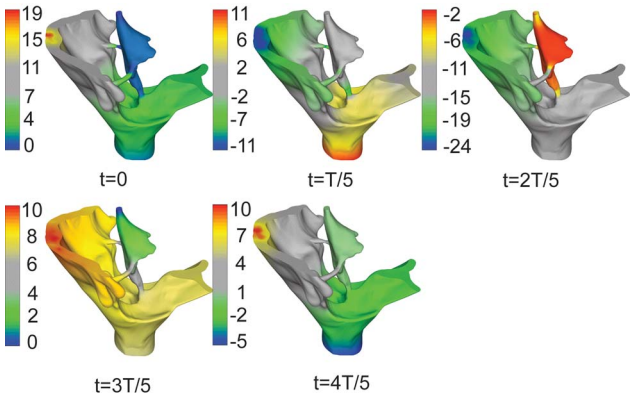

Fig. 10 Relative pressure (Pa) contours in the SAS during one complete cardiac cycle. The pressure values are given with respect to zero reference pressure at the superior end of the fourth ventricle.

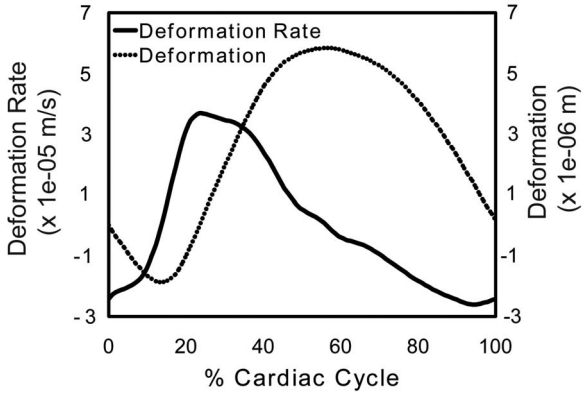

Fig. 11 Transient deformation and deformation rate of cranial SAS during one complete cardiac cycle

shown in Fig. 11. In light of these observations, the potential motion of the SAS walls has been neglected for the present analysis, yet the actual in- and outflow rates of CSF have been taken into account as measured with MRI.

An attempt has been made to capture the maximum amount of detail possible of the SAS anatomy, but the segmentation accuracy was limited by the resolution of the anatomic MRI data. It was impossible to capture the submillimeter scale structures like arachnoid granulations, which are outlets of the CSF system. These granulations are mainly present in the superior saggital sinus. They can be modeled as differential pressure valves that respond to the pressure difference across the subarachnoid space and the superior saggital sinus. Velocimetric MRI techniques (Sec. 2.2) have allowed us to capture the detailed velocity profiles in craniocaudal direction in the ponal and the cerebellar region. In general, MRI measurements detecting flow in all three directions are feasible for the domain of interest. These scans are very long and thus prone to (i) rigid body motion, (ii) heart rate changes, and (iii) respiratory motion. As the velocities of CSF are rather small, the data sets would need registration of the different velocity directions, representing a potential error source for these boundary conditions. Thus, the measurements were limited to the craniocaudal motion of the fluid at these boundaries. The knowledge of the other two velocity components, however, small they are, will be important in determining the overall accuracy of the computations. Recent publications promise accurate three-dimensional CSF flow detection to become feasible soon [52].

The accuracy of the porous media model depends on the precise structure and density of the trabeculae. The upper limit to the transverse permeability between the pia and the arachnoid layer can be assessed by a representative steady laminar flow between two parallel plates with permeability $k=D^2/12$, where D is the distance between the two plates. Assuming a small D of, for example, 1 mm, k obtains the maximum value of 8.33×10^{-8} m^2. The transverse permeability for the chosen porosity ($\varepsilon=0.99$) and trabecular radius ($r=15$ μm) becomes 2.36×10^{-8} m^2 according to Eq. (5), which is less than the upper limit. Doubling of the trabecular radius decreases the longitudinal permeability by 76%, the transverse permeability by 62%, and the porosity by 3%. This results in a total pressure variation in the entire domain from −55 Pa to 48 Pa within one cardiac cycle. Similar effects are observed with a twofold increase in trabecular density. Although the anisotropic behavior of the SAS permeability has been included in the present model, the overall resistance to fluid flow will also depend on the inclination direction of the trabeculae. In the current model, the trabeculae always extend normal to the domain walls. A detailed parametric investigation of the porous model parameters may give us more insight to this end, but we believe that the effect of inclination variation will be small because of the high porosity of the SAS.

Whenever possible, the BCs have been chosen with great emphasis on accurate reflection of the experimental velocimetric data. However, at least one pressure boundary condition is required, as pressure is determined by the incompressible Navier–Stokes equations only up to a constant [53]. For this reason, a zero pressure boundary condition has been specified at the inferior end of the aqueduct. As reliable noninvasive in vivo pressure measurements are not possible with current technology, we chose the said constant pressure BC for the sake of simplicity. The way to get rid of this virtual boundary condition is to treat the entire CSF space (ventricles and SAS) at once. However, this will significantly increase the required computational resources and will limit the detailed 3D investigation of the CSF dynamics. Furthermore, in the current study, we have assumed that there is no seepage of CSF, produced within parenchyma, through the ventricular or SAS walls. While there is no clear consensus among the CSF community on how much CSF is produced within parenchyma (extrachoroidal), the seepage, if present, would only impact the velocities near to the acqueduct or the superior fourth ventricle but will not impact our results in the SAS significantly. The reason for this is that the only place where the cerebral parenchyma surface interacts with the domain treated in this study is the entrance of the fourth ventricle, which is significantly smaller than the overall domain. Seepage would be more important in the lateral ventricles, third ventricle, and the superior cranial SAS, all of which are not part of the here treated domain.

The ultimate goal of computational biomedical models such as the one presented here is their use within a clinical environment. In such a setting, it is very important that computation times are kept as low as possible. In CFD models, a considerable amount of time can be redeemed if the grid requirements are available a priori. From the grid independence studies (Appendix A), we conclude that the boundary layer mesh used here (Sec. 2.4) was sufficient to accurately predict the flow field. The initial mesh, thus, should be chosen based on the boundary layer theory. Second, the nonconformal meshing approach should be used, as it not only allows faster grid generation but also permits replacing portions of the mesh for pathological or parametric study. In the evaluation of syringomelia, e.g., only the mesh section surrounding the cyst can be replaced as the cyst grows without having to remesh the entire domain. We have observed that flow in the superior cerebellomedullary cistern resembles a creep flow with little convection. Neglecting flow convection in the Navier–Stokes/Brinkman equations (Eq. (4)) would allow for faster flow computations.

5 Conclusions

This paper presented an original, anatomically accurate three-dimensional, transient computational model for the investigation of CSF dynamics in the inferior cranial and the superior spinal subarachnoid space. The results manifest a proof of concept for the subject specific modeling of CSF flow in the intracranial cavities. A novel porous media model incorporating anisotropic permeability variations within the trabecular SAS has been proposed. Disregarding computational cost, the model in its present form can be easily adapted to calculate CSF flow in the entire subarachnoid space. The integration of anatomic and velocimetric MRI data with computational fluid dynamics principles allowed us to reconstruct accurate velocity and pressure fields in the investigated domain.

We have provided in vivo flow information at various important cross sections within the CSF domain, some of which are otherwise inaccessible with current clinical imaging techniques. These include the flow field in the lateral and midline recesses of the fourth ventricle. Our simulations demonstrate the presence of global asymmetries in CSF flow, indicating the necessity for a three-dimensional modeling of the cerebrospinal fluid space. We have further shown that the net flow through the spinal canal in the subject at hand is negligible within one cardiac cycle, despite high-amplitude CSF oscillation. While it is not possible to draw

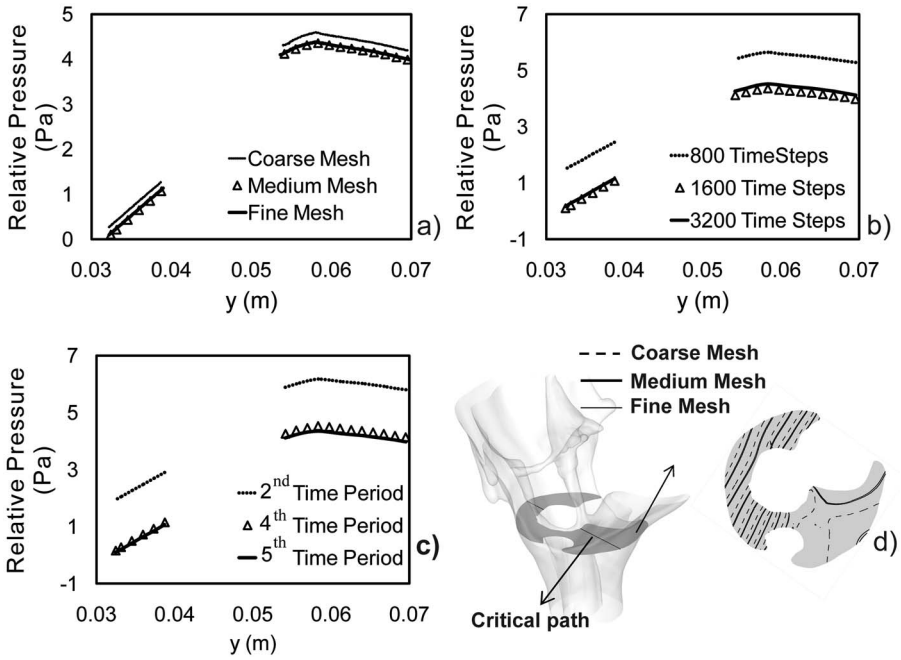

Fig. 12 Results of the independence studies. Pressure along a critical path in the treated domain as calculated (*a*) with different meshes, (*b*) at different time steps, and (*c*) with different time periods. (*d*) Pressure contours on a critical plane in the domain as calculated with different meshes.

conclusions for humans in general based on measurements of a single individual, this nevertheless shows the necessity for further investigations to see whether the net flow is truly negligible, which would indicate that CSF absorption only takes places in the cranial space. The idea of SAS deformation in the cranial cavity is an interesting finding of the current work. However, it is not yet clear whether this actually represents the global SAS deformation or only the local deformation due to deformation of blood vessels in and beneath the cranial SAS.

Our model has the potential to give better insight into various CSF related disorders. Syrinx growth in syringomyelia, e.g., is influenced by the pressure environment of the CSF in the lumbar SAS. Patient-specific variations in SAS anatomy and CSF flow caused by herniations of cerebellar tonsils in chiari malformation can be easily incorporated in the model. In addition to the study and diagnosis of cerebral diseases, intrathecal drug routing is a major potential application of this computational model. The elaborate knowledge of CSF dynamics can help optimize drug perfusion rates, penetration depth, and support targeted drug delivery.

Acknowledgment

We would like to thank Mr. John Biddiscombe and the visualization group at the Swiss National Supercomputing Center, Manno, Switzerland, for developing parallel postprocessing techniques for 3D transient visualization of CSF flow. The financial support of the ETH Zurich Research Commission has made this research possible and is kindly acknowledged.

Appendix A: Independence Studies

In order to study the effect of the spatial discretization on the CSF flow field, the computations were carried out using three levels of successively refined computational meshes. The medium mesh corresponds to boundary layer mesh (see Sec. 2.4) with 4.7×10^6 grid cells, the coarse mesh with approximately 3×10^6 grid cells, and the fine mesh with 6.6×10^6 cells. The independence tests were performed at different locations within the domain. The results presented in Fig. 12 correspond to the critical path where flow variations with spatial and temporal meshes were maximum. Figure 12(*a*) shows the pressure variation along a critical path of the domain among the three mesh sizes. Figure 12(*d*) shows the pressure contour on a critical plane for different mesh sizes. While the maximum pressure difference between the coarse mesh and the medium mesh is more than 5%, there is a very little difference between the fine and the medium mesh results, which justifies the use of the medium mesh for the calculations performed for this study. Next to grid independence, also independence of the results with respect to the number of cardiac cycles (periods) calculated and the size of the timesteps chosen was investigated. Figure 12(*c*) shows the pressure variation along a critical path for different number of periods (medium mesh, 1600 time steps per cardiac cycle). Four periods were necessary to reach period independence. Figure 12(*b*) shows the pressure variation along a critical path for different time steps. Five periods were calculated (i.e., obtaining period independence) before comparing the results obtained with 800, 600, and 3200 time steps per period. The results indicate that at least 1600 time steps are required to obtain the time step independent solution.

References

[1] Davson, H., Welch, K., Segal, M. B., and Davson, H., 1987, *Physiology and pathophysiology of the Cerebrospinal Fluid*, Churchill Livingstone, Edinburgh.
[2] Silverberg, G., Mayo, M., Saul, T., Fellmann, J., and McGuire, D., 2006, "Elevated Cerebrospinal Fluid Pressure in Patients With Alzheimer's Disease," Cerebrospinal Fluid Research, **3**(1), p. 7.
[3] Fishman, R. A., 1992, *Cerebrospinal Fluid in Diseases of the Nervous System*, Saunders, Philadelphia.
[4] Nicholson, C., 1999, "Signals That go With the Flow," Trends Neurosci., **22**(4), pp. 143–145.
[5] Kurtcuoglu, V., Soellinger, M., Summers, P., Poulikakos, D., and Boesiger, P., 2007, "Mixing and Modes of Mass Transfer in the Third Cerebral Ventricle: A Computational Analysis," ASME J. Biomech. Eng., **129**(5), pp. 695–702.
[6] Misra, A., Ganesh, S., Shahiwala, A., and Shah, S. P., 2003, "Drug Delivery to the Central Nervous System: A Review," J. Pharm. Pharm. Sci., **6**(2), pp. 252–273.
[7] Askar, F. Z., Kocabas, S., Yucel, S., Samancilar, O., Cetin, H., and Uyar, M., 2007, "The Efficacy of Intrathecal Morphine in Post-Thoracotomy Pain Management," J. Int. Med. Res., **35**(3), pp. 314–322.
[8] Lipp, J., 1991, "Possible Mechanisms of Morphine Analgesia," Clin. Neurop-

harmacol, **14**(2), pp. 131–147.
[9] Stearns, L., Boortz-Marx, R., Du Pen, S., Friehs, G., Gordon, M., Halyard, M., Herbst, L., and Kiser, J., 2005, "Intrathecal Drug Delivery for the Management of Cancer Pain: A Multidisciplinary Consensus of Best Clinical Practices," The Journal of Supportive Oncology, **3**(6), pp. 399–408.
[10] Ochiai, H., Pernell, C. T., Archer, G. E., Chewning, T. A., McLendon, R. E., Friedman, H. S., and Sampson, J. H., 2006, "Treatment of Neoplastic Meningitis With Intrathecal 9-Nitro-Camptothecin," Neurol. Med. Chir. (Tokyo), **46**(10), pp. 485–489.
[11] Richard, I., and Menei, P., 2007, "Intrathecal Baclofen in the Treatment of Spasticity, Dystonia and Vegetative Disorders," Acta Neurochir., **97**, pp. 213–218.
[12] Munsat, T. L., Taft, J., Kasdon, D., and Jackson, I. M., 1988, "Prolonged Intrathecal Infusion of Thyrotropin Releasing Hormone in Amyotrophic Lateral Sclerosis," Ann. N.Y. Acad. Sci., **531**, pp. 187–193.
[13] Drake, J. M., and Sainte-Rose, C., 1995, *The Shunt Book*, Blackwell Scientific, New York.
[14] Greitz, D., 2006, "Unraveling the Riddle of Syringomyelia," Neurosurg. Rev., **29**(4), pp. 251–263.
[15] Martin, B. A., Kalata, W., Loth, F., Royston, T. J., and Oshinski, J. N., 2005, "Syringomyelia Hydrodynamics: An In Vitro Study Based on In Vivo Measurements," ASME J. Biomech. Eng., **127**(7), pp. 1110–1120.
[16] Lakin, W. D., Stevens, S. A., Tranmer, B. I., and Penar, P. L., 2003, "A Whole-Body Mathematical Model for Intracranial Pressure Dynamics," J. Math. Biol., **46**(4), pp. 347–383.
[17] Chang, H. S., and Nakagawa, H., 2003, "Hypothesis on the Pathophysiology of Syringomyelia Based on Simulation of Cerebrospinal Fluid Dynamics," J. Neurol., Neurosurg. Psychiatry, **74**(3), pp. 344–347.
[18] Eklund, A., Smielewski, P., Chambers, I., Alperin, N., Malm, J., Czosnyka, M., and Marmarou, A., 2007, "Assessment of Cerebrospinal Fluid Outflow Resistance," Med. Biol. Eng. Comput., **45**(8), pp. 719–735.
[19] Aroussi, A., Zainy, M., and Vloeberghs, M., 2000, "Cerebrospinal Fluid Dynamics in the Aqueduct of Sylvius," *International Symposium on Flow Visualization*, pp. 1–11.
[20] Fin, L., and Grebe, R., 2003, "Three Dimensional Modeling of the Cerebrospinal Fluid Dynamics and Brain Interactions in the Aqueduct of Sylvius," Comput. Methods Biomech. Biomed. Eng., **6**(3), pp. 163–170.
[21] Jacobson, E. E., Fletcher, D. F., Morgan, M. K., and Johnston, I. H., 1996, "Fluid Dynamics of the Cerebral Aqueduct," Pediatr. Neurosurg., **24**(5), pp. 229–236.
[22] Jacobson, E. E., Fletcher, D. F., Morgan, M. K., and Johnston, I. H., 1999, "Computer Modelling of the Cerebrospinal Fluid Flow Dynamics of Aqueduct Stenosis," Med. Biol. Eng. Comput., **37**(1), pp. 59–63.
[23] Kurtcuoglu, V., Poulikakos, D., and Ventikos, Y., 2005, "Computational Modeling of the Mechanical Behavior of the Cerebrospinal Fluid System," ASME J. Biomech. Eng., **127**(2), pp. 264–269.
[24] Kurtcuoglu, V., Soellinger, M., Summers, P., Boomsma, K., Poulikakos, D., Boesiger, P., and Ventikos, Y., 2005, "Reconstruction of Cerebrospinal Fluid Flow in the Third Ventricle Based on MRI Data," Medical Image Computing and Computer-Assisted Intervention—MICCAI 2005: 8th International Conference, Palm Springs, Lect. Notes Comput. Sci., **3749**, pp. 786–793.
[25] Kurtcuoglu, V., Soellinger, M., Summers, P., Boomsma, K., Poulikakos, D., Boesiger, P., and Ventikos, Y., 2007, "Computational Investigation of Subject-Specific Cerebrospinal Fluid Flow in the Third Ventricle and Aqueduct of Sylvius," J. Biomech., **40**(6), pp. 1235–1245.
[26] Jacobson, E. E., Fletcher, D. F., Johnston, I. H., and Morgan, M. K., 1999, "Computer Modelling of CSF Flow in the Subarachnoid Space," J. Neuropsychiatry Clin. Neurosci., **6**(6), pp. 498–500.
[27] Loth, F., Yardimci, M. A., and Alperin, N., 2001, "Hydrodynamic Modeling of Cerebrospinal Fluid Motion Within the Spinal Cavity," ASME J. Biomech. Eng., **123**(1), pp. 71–79.
[28] Stockman, H. W., 2006, "Effect of Anatomical Fine Structure on the Flow of Cerebrospinal Fluid in the Spinal Subarachnoid Space," ASME J. Biomech. Eng., **128**(1), pp. 106–114.
[29] Zhu, D. C., Xenos, M., Linninger, A. A., and Penn, R. D., 2006, "Dynamics of Lateral Ventricle and Cerebrospinal Fluid in Normal and Hydrocephalic Brains," J. Magn. Reson Imaging, **24**(4), pp. 756–770.
[30] Linninger, A. A., Xenos, M., Zhu, D. C., Somayaji, M. R., Kondapalli, S., and Penn, R. D., 2007, "Cerebrospinal Fluid Flow in the Normal and Hydrocephalic Human Brain," IEEE Trans. Biomed. Eng., **54**(2), pp. 291–302.
[31] Linninger, A. A., Tsakiris, C., Zhu, D. C., Xenos, M., Roycewicz, P., Danziger, Z., and Penn, R., 2005, "Pulsatile Cerebrospinal Fluid Dynamics in the Human Brain," IEEE Trans. Biomed. Eng., **52**(4), pp. 557–565.
[32] Killer, H. E., Laeng, H. R., Flammer, J., and Groscurth, P., 2003, "Architecture of Arachnoid Trabeculae, Pillars, and Septa in the Subarachnoid Space of the Human Optic Nerve: Anatomy and Clinical Considerations," Br. J. Ophthamol., **87**(6), pp. 777–781.
[33] Tada, Y., and Nagashima, T., 1994, "Modeling and Simulation of Brain-Lesions by the Finite-Element Method," IEEE Eng. Med. Biol. Mag., **13**(4), pp. 497–503.
[34] Pinna, G., Alessandrini, F., Alfieri, A., Rossi, M., and Bricolo, A., 2000, "Cerebrospinal Fluid Flow Dynamics Study in Chiari I Malformation: Implications for Syrinx Formation," Neurosurg. Focus, **8**(3), p. E3.
[35] Lim, J. S., 1990, *Two-Dimensional Signal and Image Processing*, Prentice-Hall International, London.
[36] Brinkman, H. C., 1948, "On the Permeability of Media Consisting of Closely Packed Porous Particles," Appl. Sci. Res., Sect. A, **1**(2), pp. 81–86.
[37] Vandenwesthuizen, J., and Duplessis, J. P., 1994, "Quantification of Unidirectional Fiber Bed Permeability," J. Compos. Mater., **28**(7), pp. 619–637.
[38] Boomsma, K., Poulikakos, D., and Ventikos, Y., 2003, "Simulations of Flow Through Open Cell Metal Foams Using an Idealized Periodic Cell Structure," Int. J. Heat Fluid Flow, **24**(6), pp. 825–834.
[39] Prieur du Plessis, J., 1997, *Fluid Transport in Porous Media*, Computational Mechanics, Southampton.
[40] Warming, R. F., and Beam, R. M., 1976, "Upwind 2nd-Order Difference Schemes and Applications in Aerodynamic Flows," AIAA J., **14**(9), pp. 1241–1249.
[41] Vandoormaal, J. P., and Raithby, G. D., 1984, "Enhancements of the Simple Method for Predicting Incompressible Fluid-Flows," Numer. Heat Transfer, **7**(2), pp. 147–163.
[42] Rauch, R. D., Batira, J. T., and Yang., N. T. Y., 1991, "Spatial Adaption Procedures on Unstructured Meshes for Accurate Unsteady Aerodynamic Flow Computations," AIAA Paper No. AIAA-91-1106.
[43] Hayman, L. A., Evans, R. A., and Hinck, V. C., 1979, "Choroid Plexus of the Fourth Ventricle: A Useful CT Landmark," AJR, Am. J. Roentgenol., **133**(2), pp. 285–288.
[44] Pope, W., 1998, "External Ventriculostomy: A Practical Application for the Acute Care Nurse," J. Neurosci. Nurs., **30**(3), pp. 185–190.
[45] Toga, A. W., and Thompson, P. M., 2003, "Mapping Brain Asymmetry," Nature Reviews Neuroscience, **4**(1), pp. 37–48.
[46] Gideon, P., Stahlberg, F., Thomsen, C., Gjerris, F., Sorensen, P. S., and Henriksen, O., 1994, "Cerebrospinal Fluid Flow and Production in Patients With Normal Pressure Hydrocephalus Studied by MRI," Neurosci. Res. (N Y), **36**(3), pp. 210–215.
[47] Silverberg, G. D., Heit, G., Huhn, S., Jaffe, R. A., Chang, S. D., Bronte-Stewart, H., Rubenstein, E., Possin, K., and Saul, T. A., 2001, "The Cerebrospinal Fluid Production Rate is Reduced in Dementia of the Alzheimer'S Type," Neurology, **57**(10), pp. 1763–1766.
[48] Feinberg, D. A., and Mark, A. S., 1987, "Human Brain Motion and Cerebrospinal Fluid Circulation Demonstrated With MR Velocity Imaging," Radiology, **163**(3), pp. 793–799.
[49] Greitz, D., 2004, "Radiological Assessment of Hydrocephalus: New Theories and Implications for Therapy," Neurosurg. Rev., **27**(3), pp. 145–165.
[50] Soellinger, M., Ryf, S., Boesiger, P., and Kozerke, S., 2007, "Assessment of Human Brain Motion Using CSPAMM," J. Magn. Reson Imaging, **25**(4), pp. 709–714.
[51] Soellinger, M., Rutz, A., Boesiger, P., and Kozerke, S., 2007, "Time-Resolved, Three-Dimensional Brain Motion Measurements Using 3D-DENSE," Proc. Intl. Soc. Mag. Reson. Med., **15**, 3005, 15th Scientific Meeting of the International Society of Magnetic Resonance Imaging in Medicine (ISMRM), Berlin, Germany, May 19–25.
[52] Wetzel, S., Meckel, S., Frydrychowicz, A., Bonati, L., Radue, E. W., Scheffler, K., Hennig, J., and Markl, M., 2007, "In Vivo Assessment and Visualization of Intracranial Arterial Hemodynamics With Flow-Sensitized 4D MR Imaging at 3T," AJNR Am. J. Neuroradiol., **28**(3), pp. 433–438.
[53] Gresho, P. M., and Sani, R. L., 1987, "On Pressure Boundary-Conditions for the Incompressible Navier–Stokes Equations," Int. J. Numer. Methods Fluids, **7**(10), pp. 1111–1145.